



Atomistic modeling of surface and grain boundary dislocation nucleation in FCC metals

Yin Zhang^{a,1}, Kunqing Ding^{a,1}, Sandra Stangebye^b, Dengke Chen^a, Josh Kacher^b, Olivier Pierron^a, Ting Zhu^{a,b,*}

^a Woodruff School of Mechanical Engineering, Georgia Institute of Technology, Atlanta, GA, 30332, USA

^b School of Materials Science and Engineering, Georgia Institute of Technology, Atlanta, GA, 30332, USA



ARTICLE INFO

Article history:

Received 5 June 2022

Accepted 5 July 2022

Available online 12 July 2022

Keywords:

Grain boundary

Dislocation nucleation

Activation volume

ABSTRACT

Dislocation nucleation plays a critical role in the plastic deformation of crystalline materials. However, it is challenging to predict the active mode and associated rate of dislocation nucleation under typical experimental loading conditions through molecular dynamics simulation due to timescale limitations. Here we use the free-end nudged elastic band method to determine the activation energies and activation volumes of dislocation nucleation in four typical face-centered cubic metals of Au, Al, Cu and Ni. We focus on the representative processes of surface and grain boundary dislocation nucleation. The atomistically determined activation volumes of these dislocation nucleation processes are larger than $10b^3$ (with b being the Burgers vector length) under typical experimental loading conditions. These results are compared with experimentally measured activation volumes in ultrafine-grained and nanocrystalline metals, thereby providing mechanistic insight into their rate-controlling deformation mechanisms.

© 2022 Acta Materialia Inc. Published by Elsevier Ltd. All rights reserved.

1. Introduction

Dislocations usually serve as plastic deformation carriers of crystalline materials [1,2]. In coarse-grained face-centered cubic (FCC) metals, plastic flow is controlled by dislocation interactions with grain boundaries and other obstacles. However, the confined volume in nanostructured FCC metals can largely suppress dislocation interactions, leading to dislocation nucleation-controlled plastic flow [3,4]. Dislocation nucleation is typically a stress-driven, thermally-activated rare event. It is difficult to predict the active mode and associated rate of dislocation nucleation under typical experimental loading conditions through direct molecular dynamics (MD) simulation due to timescale limitations. To address this issue, one effective approach is to predict the rate of dislocation nucleation based on transition state theory [1]

$$v = v_0 \exp\left(-\frac{\Delta G(\tau, T)}{k_B T}\right) \quad (1)$$

where v_0 is the trial frequency, ΔG is the activation free energy, τ is the applied resolved shear stress on the dislocation slip system, T is the temperature, and k_B is the Boltzmann constant. The trial frequency v_0 for a dislocation line is on the order of 10^{11} s^{-1} [5],

as dictated by atomic vibration. To match the nucleation rate with a typical laboratory strain rate of 10^{-3} s^{-1} , ΔG of a rate-controlling dislocation process should be approximately $30k_B T$, which corresponds to 0.7 eV at room temperature [6]. The temperature effect on ΔG in Eq. (1) can be incorporated into the prefactor v_0 based on harmonic transition state theory [7]. Hence, we refer to the temperature-independent part of ΔG as the activation energy $E_{\text{act}}(\tau)$ that depends only on stress. One can calculate $E_{\text{act}}(\tau)$ by exploring the potential energy surface of an atomic system using the nudged elastic band (NEB) method [8–11].

In addition to the activation energy, the activation volume is another key activation parameter of dislocation nucleation. In particular, it can be used to identify the critical process of dislocation nucleation, among various candidate processes, that controls the rate of plastic flow under typical experimental loading conditions. The activation volume, V_{exp} , can be obtained from experimental tensile tests according to

$$V_{\text{exp}} = \sqrt{3}k_B T \frac{\partial \ln \dot{\epsilon}}{\partial \sigma} \quad (2)$$

where $\dot{\epsilon}$ is the tensile strain rate and σ is the tensile stress. In Eq. (2), the factor of $\sqrt{3}$ is used to convert the tensile stress to the effective shear stress driving a rate-controlling dislocation process. The activation volume has been measured to determine the strength/rate-controlling mechanisms governing the plastic flow of polycrystalline metals [12,13]. This approach is widely used in the

* Corresponding author.

E-mail address: ting.zhu@me.gatech.edu (T. Zhu).

¹ These authors contributed equally

study of coarse-grained materials [1,2] and has recently been extended to study ultrafine-grained and nanocrystalline metals [14–20]. However, the currently available experimental results of activation volumes for ultrafine-grained and nanocrystalline metals are limited and, more importantly, puzzling, as to be discussed below.

To determine the activation volume by atomistic modeling, a series of NEB calculations can be performed to determine $E_{\text{act}}(\tau)$ for a candidate rate-controlling dislocation process at different stresses. The activation volume from modeling, denoted as V_{mod} , is obtained as [10]

$$V_{\text{mod}} = -\frac{\partial E_{\text{act}}(\tau)}{\partial \tau} \quad (3)$$

One can further calculate activation volumes for different candidate dislocation processes. These atomistically determined activation volumes usually have characteristically different values and thus can be compared with the experimentally measured activation volume for determining the critical dislocation process that controls the rate of plastic flow [3].

Past modeling studies have reported the activation energies of dislocation processes in metals [9–11, 21–29], but the corresponding studies of activation volumes are much limited [10,11]. In light of the increasing experimental reports of activation volumes in ultrafine-grained and nanocrystalline metals [15–20], we focus on the atomistic determination of activation energies and particularly activation volumes of dislocation nucleation in FCC metals. We study two typical nucleation scenarios, i.e., surface nucleation in nano-sized single crystals and grain boundary (GB) nucleation in nano-sized bi-crystals under the same effective loading direction. The NEB method is used to determine the minimum energy path (MEP) and associated saddle-point state and activation energy of each nucleation process under an applied stress. Our systematic NEB results give the stress-dependent activation energies that are used to calculate the stress-dependent activation volumes. These studies are performed for four typical FCC metals of Al, Ni, Cu and Au, considering their markedly different material properties, i.e., shear modulus, Burgers vector length and stacking fault energy, in order to develop a general understanding of dislocation nucleation in FCC metals. Note that the free-end NEB (FENE) method [10] is used to capture the saddle-point state with high computational efficiency, and recent implementation of the FENE method in LAMMPS [30] can facilitate the verification and extension of our results by other research groups. In addition, we perform a theoretical analysis of dislocation nucleation to clarify the effect of material properties on activation energy and activation volume. We also adapt a stress concentration model to account for the grain size effect on activation volumes. This model is essential for connecting the atomistically determined activation volumes at GBs with the experimentally measured activation volumes from polycrystalline samples. Moreover, we discuss other possible diffusive dislocation processes that may compete with the displacive dislocation processes, thereby offering a broader perspective on the experimentally measured activation volumes and associated rate-controlling mechanisms.

2. Methods

To study surface dislocation nucleation, we use single-crystal nanowires of Au, Al, Cu and Ni with the same orientation and geometry (rescaled by lattice constant). For example, Fig. 1(a) shows the atomic structure of an Au sample, which has the dimension of $16.3 \text{ nm} \times 9.8 \text{ nm} \times 9.7 \text{ nm}$ and contains 102,600 atoms. The periodic boundary condition and tensile strain load are imposed along the axial direction of $[4\bar{1}5]$. The side surfaces of (111) and $(2\bar{3}1)$ are traction free. Since dislocations in FCC metals dissociate into partial dislocations, we focus on the surface nucleation of a lead-

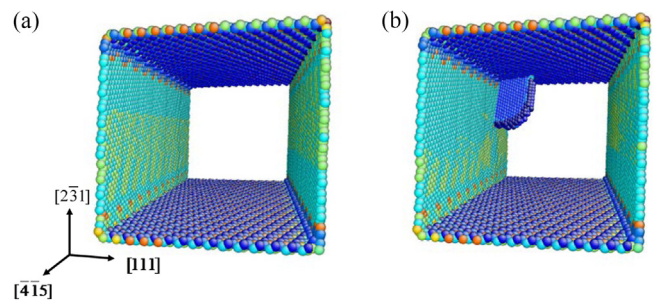


Fig. 1. Atomistic FENE simulation setup for surface dislocation nucleation in an Au single crystal. (a) An initial defect-free configuration. (b) A typical free-end state with an embryonic partial dislocation loop at the sample corner.

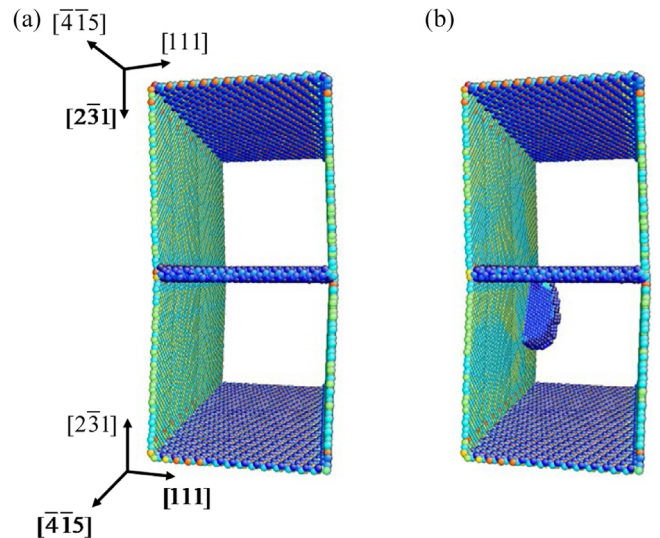


Fig. 2. Atomistic FENE simulation setup for GB dislocation nucleation in an Au bi-crystal. (a) An initial defect-free configuration containing a symmetric tilt GB with the tilt axis of $[111]$ and the GB plane of $(2\bar{3}1)$. The tensile load is applied on $[4\bar{1}5]$ direction. (b) A typical free-end state with an embryonic partial dislocation loop at the intersection between the GB and surface.

ing partial dislocation. The MEP of surface nucleation is calculated using the FENE method in LAMMPS [30] with an embedded atom method (EAM) potential of Au [31]. We focus on the surface nucleation from a corner of the sample. The embryonic dislocation glides on a $[111]\langle 112 \rangle$ slip system with the largest Schmid factor of 0.41. We first obtain an approximate MEP of surface nucleation using the traditional NEB method, which requires the initial and end states as local minima. To control this targeted mode of surface nucleation, we embed a surface dislocation loop by a locally-controlled shearing method [11]. After this traditional NEB calculation, we locate the replica whose energy is close to the energy of the initial state and use that configuration as the final “free-end” configuration (Fig. 1(b)) in a FENE calculation. Then a series of FENE calculations are performed under different applied tensile strains. For each FENE calculation, the replicas along the guessed MEP are setup by applying an incremental strain to the replicas from a previously converged FENE calculation at a lower strain load. We also perform FENE calculations for the same mode of surface dislocation nucleation in Al, Cu and Ni with the corresponding EAM potential [32–34]. The atomic configurations presented in this work are visualized by the centrosymmetry coloring scheme in AtomEye [35], so as to clearly display atoms on the surface, GB and stacking fault.

To study GB dislocation nucleation, we use bi-crystal nanowires of Au, Al, Cu and Ni. For example, we set up a bi-crystal Au

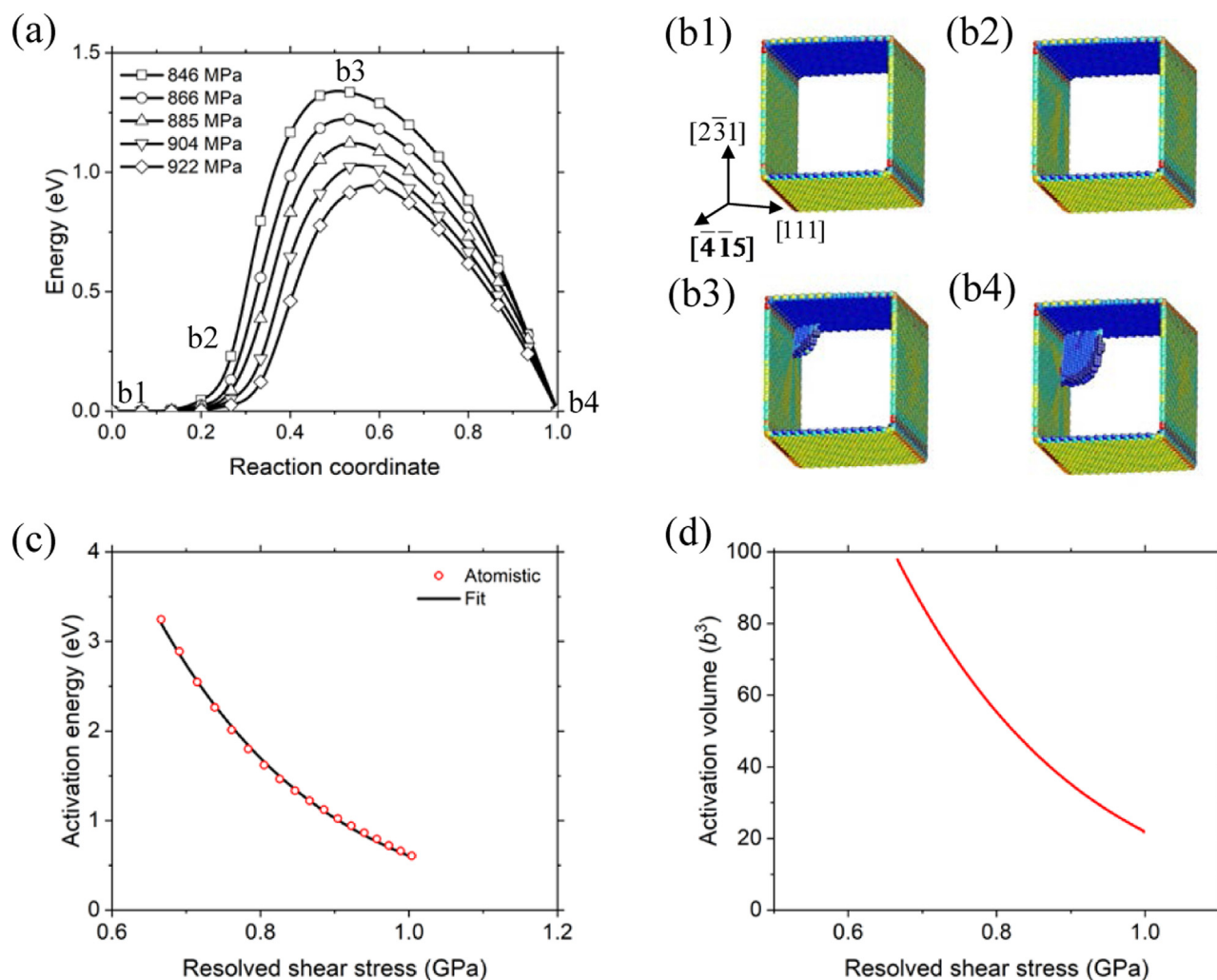


Fig. 3. FENEb results for surface dislocation nucleation from the corner of an Au single crystal. (a) MEPs at different applied resolved shear stresses. Each set of symbols (e.g., squares) represents the energies of replicas along the MEP under an applied resolved shear stress. (b1–b4) Atomic configurations (marked in (a)) along the MEP under an applied resolved shear stress of 846 MPa, showing the saddle-point state of surface nucleation (b3). (c) Activation energy as a function of resolved shear stress. Circles represent the FENEb results and the solid line is the fitting curve. (d) Activation volume as a function of resolved shear stress, obtained using Eq. (3) and the fitting curve in (c).

sample containing a symmetric tilt GB with the tilt axis of $[111]$ and the GB plane of $(2\bar{3}1)$, as shown in Fig. 2. This $[111]$ tilt GB is taken as a representative GB in the $[111]$ -textured Au sample used in experiments [18]. More specifically, we start with a crystal of the same orientation as the single-crystal nanowire, corresponding to the lower half of the bi-crystal in Fig. 2(a). The upper half of the bi-crystal is constructed by mirror-reflection of the lower half about its side surface of $(2\bar{3}1)$. As a result, the GB plane is $(2\bar{3}1)$, and the symmetric upper and lower crystals have a misorientation of 21.8° . The bi-crystal Au sample has the dimension of $16.3 \text{ nm} \times 32.8 \text{ nm} \times 20.6 \text{ nm}$ and contains 226,260 atoms. The periodic boundary condition is imposed along the loading direction of $[\bar{4}\bar{1}5]$. The two side surfaces of (111) and $(2\bar{3}1)$ are traction free. The GB structure is relaxed by energy minimization with the conjugate gradient method. The GB dislocation nucleation mode studied in the $[\bar{4}\bar{1}5]$ grain involves the same nucleation site and activated slip system as the study of surface dislocation nucleation in the $[\bar{4}\bar{1}5]$ -oriented single-crystal nanowire. Fig. 2(b) shows a typical “free-end” configuration in an FENEb calculation. The MEPs of GB dislocation nucleation are determined by FENEb calculations at different applied tensile stresses. In our NEB calculations, the favored nucleation site is at

the GB-free surface junction, consistent with our MD simulation results.

3. Results

Surface dislocation nucleation. Fig. 3 shows the FENEb results of surface dislocation nucleation in Au. In Fig. 3(a), we plot five representative MEPs under different resolved shear stresses, τ , on the activated $\{111\}\langle 112\rangle$ slip system, which are calculated from the corresponding tensile stresses applied to the nanowire. Fig. 3(b) shows the dislocation structures along the MEP corresponding to $\tau = 846 \text{ MPa}$ in Fig. 3(a). An embryonic partial dislocation loop initially nucleates from a corner of the nanowire (Fig. 3(b3)). This embryonic loop subsequently expands towards the other side of the free surface (Fig. 3(b4)). In the saddle-point configuration of Fig. 3(b3), the loop shape is close to a quarter of a circle. The small plate of blue atoms corresponds to the stacking fault; and the partial dislocation core is along the edge of the stacking fault. The energy of this saddle-point state is the maximum (marked as “b3”) on the corresponding MEP in Fig. 3(a), giving the activation energy $E_{\text{act}} = 1.33 \text{ eV}$ at $\tau = 846 \text{ MPa}$.

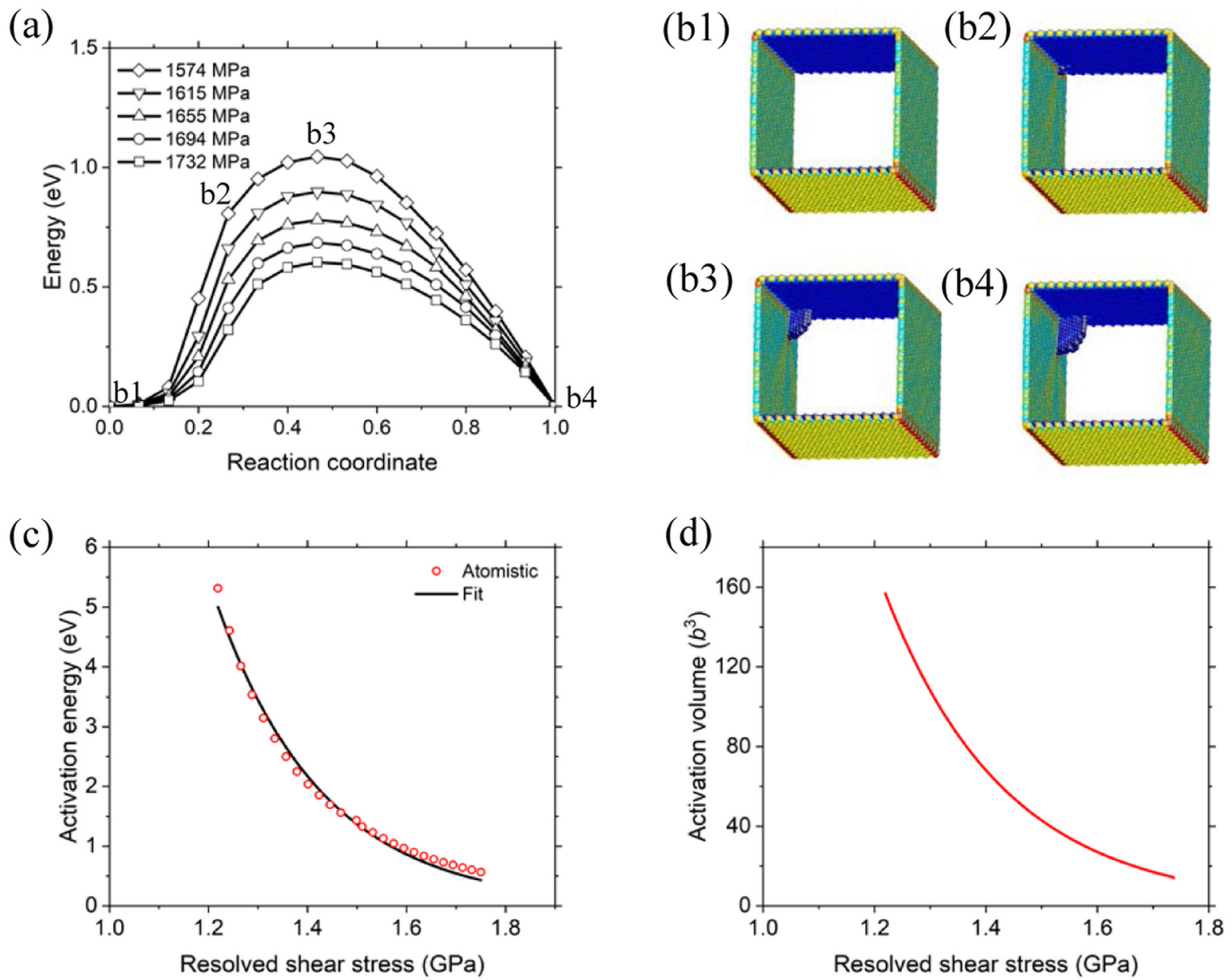


Fig. 4. FENEb results for surface dislocation nucleation from the corner of an Al single crystal. (a) MEPs at different applied resolved shear stresses. (b1–b4) Atomic configurations along the MEP, marked in (a), at an applied resolved shear stress of 1574 MPa. (c) Stress-dependent activation energy as a function of resolved shear stress. Circles show the FENEb results and the solid line is the fitting curve. (d) Activation volume as a function of resolved shear stress.

The stress-dependent activation energies $E_{act}(\tau)$ are shown in Fig. 3(c), where the circles represent direct FENEb results and the solid line is a fitting curve by the form $E_{act}(\tau) = A(1 - \tau/\tau_{ath})^d$ [11], with the fitting parameters of $A_{Au} = 46.2$ eV, $\tau_{ath,Au} = 2848$ MPa, and $d_{Au} = 10$ for the Au nanowire. As discussed earlier, the dislocation process with a characteristic E_{act} value of 0.7 eV underlies the typical laboratory strain rate of 10^{-3} s $^{-1}$ at room temperature. From Fig. 3(c), the resolved shear stress τ giving $E_{act} = 0.7$ eV is determined to be 1.1 GPa. In addition, we obtain the activation volumes $V_{mod}(\tau)$ based on Eq. (3), using the fitting curve for $E_{act}(\tau)$. Fig. 3(d) shows the V_{mod} vs. τ curve, where V_{mod} is normalized by a characteristic atomic volume of b^3 (with $b = 0.289$ nm which is the full dislocation Burgers vector length of Au). Similar to E_{act} , V_{mod} also decreases with increasing τ . Corresponding to $E_{act} = 0.7$ eV at $\tau = 0.97$ GPa, V_{mod} is $\sim 20b^3$. This characteristic activation volume V_{mod} for surface dislocation nucleation will be compared with that for GB dislocation nucleation, in order to correlate these modeling results with the corresponding experimental measurements of Au.

To study the same mode of surface dislocation nucleation in Al, the atomic configuration of the Al nanowire is set up by rescaling that of the Au nanowire based on the corresponding lattice constants in Table 1. Fig. 4 shows the FENEb results of surface dislocation nucleation in the Al nanowire, including MEPs in Fig. 4(a),

Table 1

Material properties given by the interatomic potentials of Au, Al, Cu and Ni [31–34] used in this work, including the shear modulus $\mu = (C_{11} - C_{12} + C_{44})/3$ (where C_{11} , C_{12} and C_{44} are the single-crystal elastic constants), Burgers vector length b , characteristic energy μb^3 and stacking fault energy γ_{SF} .

	μ (GPa)	b (nm)	μb^3 (eV)	γ_{SF} (mJ/m 2)
Au	23.7	0.288	3.53	2
Al	28.0	0.286	4.09	146
Cu	41.2	0.256	4.31	45
Ni	74.7	0.249	7.20	125

atomic configurations along a representative MEP in Fig. 4(b), stress-dependent activation energies in Fig. 4(c) and activation volumes in Fig. 4(d). To attain $E_{act} = 0.7$ eV for Al, the corresponding resolved shear stress τ is 1.7 GPa and the activation volume V_{mod} is $\sim 20b^3$. Comparison of Fig. 3(c) and Fig. 4(c) shows that attaining the same value of E_{act} requires a higher resolved shear stress τ for Al than Au. This can be attributed mainly to the higher shear modulus μ of Al than Au (Table 1). Further comparison of the Au and Al results is given below.

We also perform FENEb calculations to study the same nucleation mode in Ni and Cu. Fig. 5 shows the comparison of FENEb results of surface dislocation nucleation for Al, Ni, Cu and Au. Note

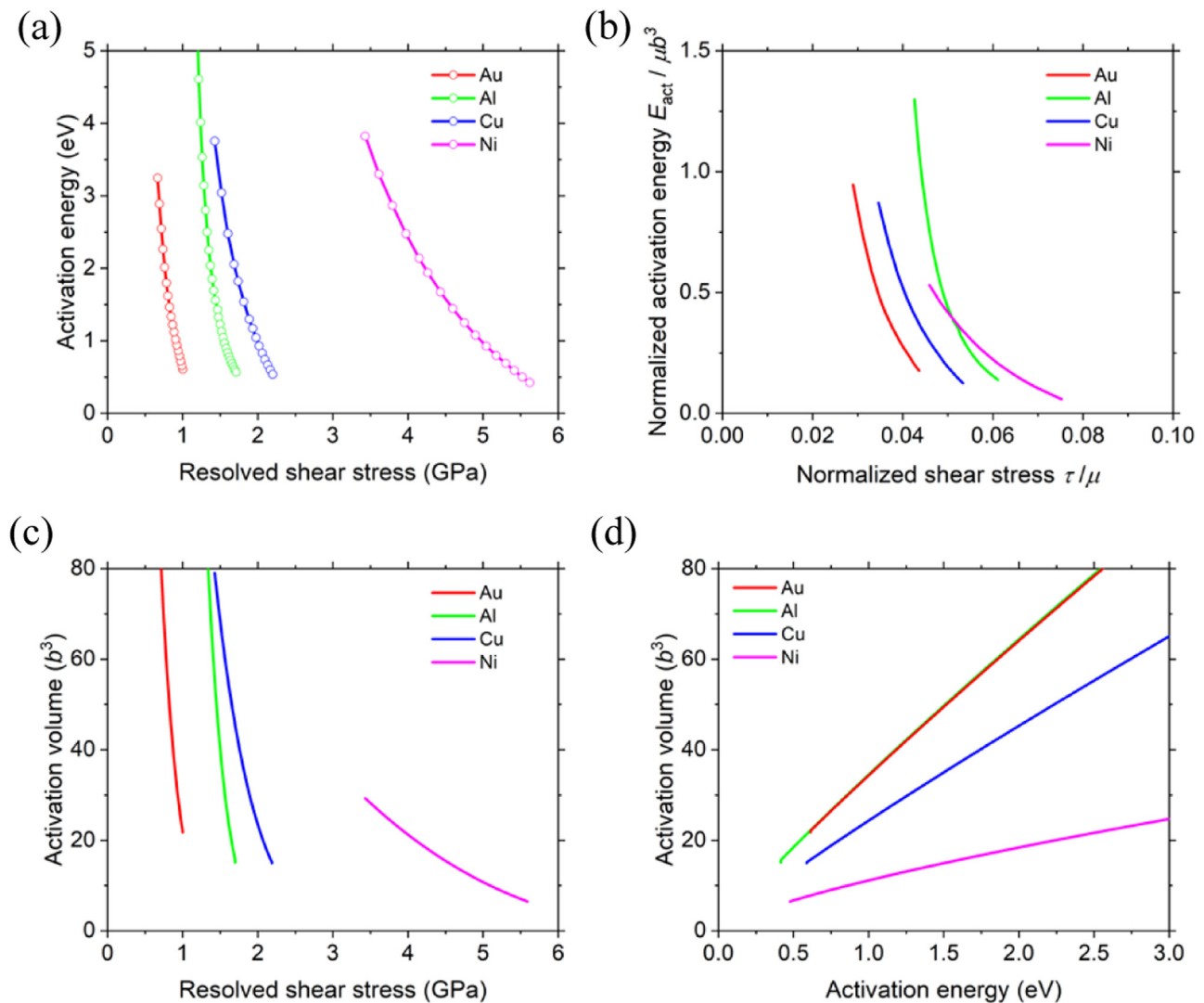


Fig. 5. Comparison of FENEb results for surface dislocation nucleation in Au, Al, Cu and Ni. (a) Activation energy E_{act} vs. resolved shear stress τ . Circles represent the FENEb results and solid lines are the fitting curves. (b) Normalized activation energy $E_{act}/\mu b^3$ vs. normalized shear stress τ/μ . (c) Activation volume V_{mod}/b^3 vs. resolved shear stress τ . (d) Activation volume V_{mod}/b^3 vs. activation energy E_{act} .

that the FENEb calculations for each metal can only retain the same mode of nucleation in a certain load range, such that varying ranges of activation energies and activation volumes are obtained for the four metals, as plotted in Fig. 5. In other words, an applied load that is outside a certain range will result in the converged MEP of a different nucleation mode that cannot be used for comparison. In Fig. 5(a), we compare the E_{act} vs. τ curves for the same nucleation mode in the four metals. To attain the same E_{act} value, τ for Ni is the highest due to its highest shear modulus (Table 1). However, the corresponding V_{mod} (magnitude of slope in Fig. 5(a)) is the lowest among the four metals, suggesting a more rate-sensitive behavior associated with surface dislocation nucleation in Ni. Fig. 5(b) shows the normalized activation energy $E_{act}/\mu b^3$ vs. normalized resolved shear stress τ/μ . Note that μb^3 represents a characteristic measure of the elastic energy associated with a dislocation line (see Table 1). Compared to Fig. 5(a), Fig. 5(b) shows that the $E_{act}/\mu b^3$ vs. τ/μ curves of the four metals become much closer to each other. This result indicates a consistent dependence of the normalized activation energy of surface dislocation nucleation on the normalized resolved shear stress for the four metals, a general trend that is conceivably applicable to other FCC metals. It also indicates that the shear modulus and atomic

spacing (through Burgers vector) are the primary factors governing the nucleation barriers, whereas other material properties, such as stacking fault energy, surface energy and elastic anisotropy, play secondary roles. In Fig. 5(c), we compare the V_{mod} vs. τ curves for the four metals. Ni exhibits relatively low values of V_{mod} with a weak dependence on τ compared to the other three metals. In Fig. 5(d), we compare the V_{mod} vs. E_{act} curves for the four metals. Corresponding to $E_{act} = 0.7$ eV, Au, Al and Cu have similar activation volumes around $20b^3$, whereas Ni has a smaller activation volume of around $10b^3$. In addition, Fig. 5(d) shows that for the same activation energy, the corresponding activation volume decreases with increasing shear modulus in Au, Cu, and Ni. However, Al deviates from this trend, as shown by the coincidentally overlapping V_{mod}/b^3 vs. E_{act} curves between Al and Au. This deviation could be attributed to stronger directional bonding in Al than other FCC metals, which is manifested by its unusual elastic shear stress-strain behavior, namely, a markedly larger shear strain limit before the decrease of shear stress [36].

GB dislocation nucleation. Fig. 6 shows the FENEb results of GB dislocation nucleation in Au. In Fig. 6(a), we plot five representative MEPs at different resolved shear stresses, τ , on the activated $\{111\}\langle 112 \rangle$ slip system in the $[\bar{4}15]$ grain. Fig. 6(b) shows the dis-

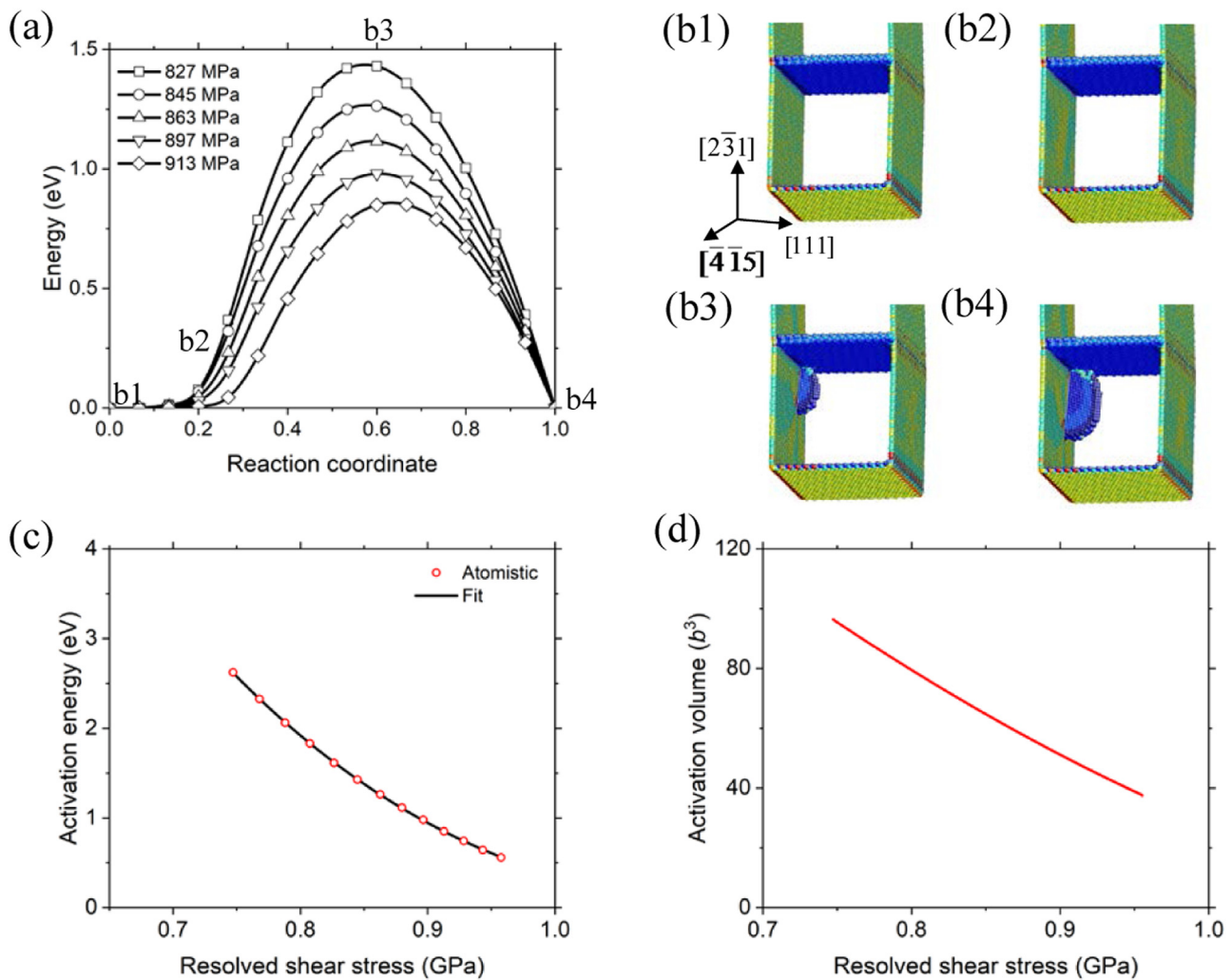


Fig. 6. FENEb results for GB dislocation nucleation in an Au bi-crystal. (a) MEPs at different applied resolved shear stresses. (b1–b4) Atomic configurations (marked in (a)) along the MEP under an applied resolved shear stress of 827 MPa, showing the saddle-point state of GB nucleation (b3). (c) Activation energy as a function of resolved shear stress. Circles represent the FENEb results and the solid line is the fitting curve. (d) Activation volume as a function of resolved shear stress.

location structures along the MEP at $\tau = 827$ MPa in Fig. 6(a). It is seen that an embryonic loop emanates from a corner between the GB and grain surface. In contrast to the nearly isotropic shape of the surface-nucleated loop in Fig. 3(b), the dislocation loop in Fig. 6(b) is elongated perpendicular to the GB. This is caused by different glide resistances to the loop intersection points at the GB and grain surface. The stress-dependent activation energies $E_{\text{act}}(\tau)$ are shown in Fig. 6(c), where the circles represent direct FENEb results and the solid line is a fitting curve. Corresponding to $E_{\text{act}} = 0.7$ eV, τ is 0.93 GPa. This stress is lower than 0.97 GPa needed for surface dislocation nucleation, indicating the relative ease of GB dislocation nucleation. Fig. 6(d) shows the V_{mod} vs. τ curve for Au. Corresponding to $E_{\text{act}} = 0.7$ eV at $\tau = 0.93$ GPa, the activation volume V_{mod} is $\sim 50b^3$, which is more than twice V_{mod} for the corresponding process of surface dislocation nucleation. The favored activation of this nucleation mode is confirmed by direct MD simulations under higher stresses than those applied in FENEb calculations.

Fig. 7 shows the FENEb results of GB dislocation nucleation in a bi-crystal Al nanowire. The difference of GB dislocation nucleation between Au and Al is qualitatively similar to that of surface dislocation nucleation. Corresponding to $E_{\text{act}} = 0.7$ eV at $\tau = 1.60$ GPa, V_{mod} is $\sim 16b^3$ for Al. We also perform FENEb calculations to study

the same nucleation mode in Ni and Cu. Fig. 8 shows comparison of the FENEb results of GB dislocation nucleation for the four metals. The E_{act} vs. τ curves are compared in Fig. 8(a), and the corresponding normalized curves in Fig. 8(b). In addition, we show the V_{mod} vs. τ curves in Fig. 8(c), and the V_{mod} vs. E_{act} curves in Fig. 8(d). Comparison of Figs. 5 and 8 indicates that both the overall trend for the same metal and the relative changes among different FCC metals are qualitatively consistent between GB and surface dislocation nucleation. However, there are notable quantitative differences. For example, as shown in Fig. 5(a), attaining the same E_{act} value such as 0.7 eV for surface dislocation nucleation requires $\tau = 0.97$ GPa for Au, 1.60 GPa for Al, 2.12 GPa for Cu, and 5.28 GPa for Ni. In comparison, as shown in Fig. 8(a), attaining the same E_{act} value such as 0.7 eV for GB dislocation nucleation requires $\tau = 0.93$ GPa for Au, 1.78 GPa for Al, 2.23 GPa for Cu, and 5.09 GPa for Ni. In addition, the activation volumes of GB dislocation nucleation in Au become larger than those for surface dislocation nucleation, as seen from Figs. 5(d) and 8(d). For example, corresponding to $E_{\text{act}} = 0.7$ eV, the activation volume V_{mod} increases from $20b^3$ for surface dislocation nucleation to $50b^3$ for GB dislocation nucleation in Au. Also note that the V_{mod} vs. E_{act} curve for GB dislocation nucleation in Au is shifted away from the curves of the other three metals, reflecting larger activation volumes in Au.

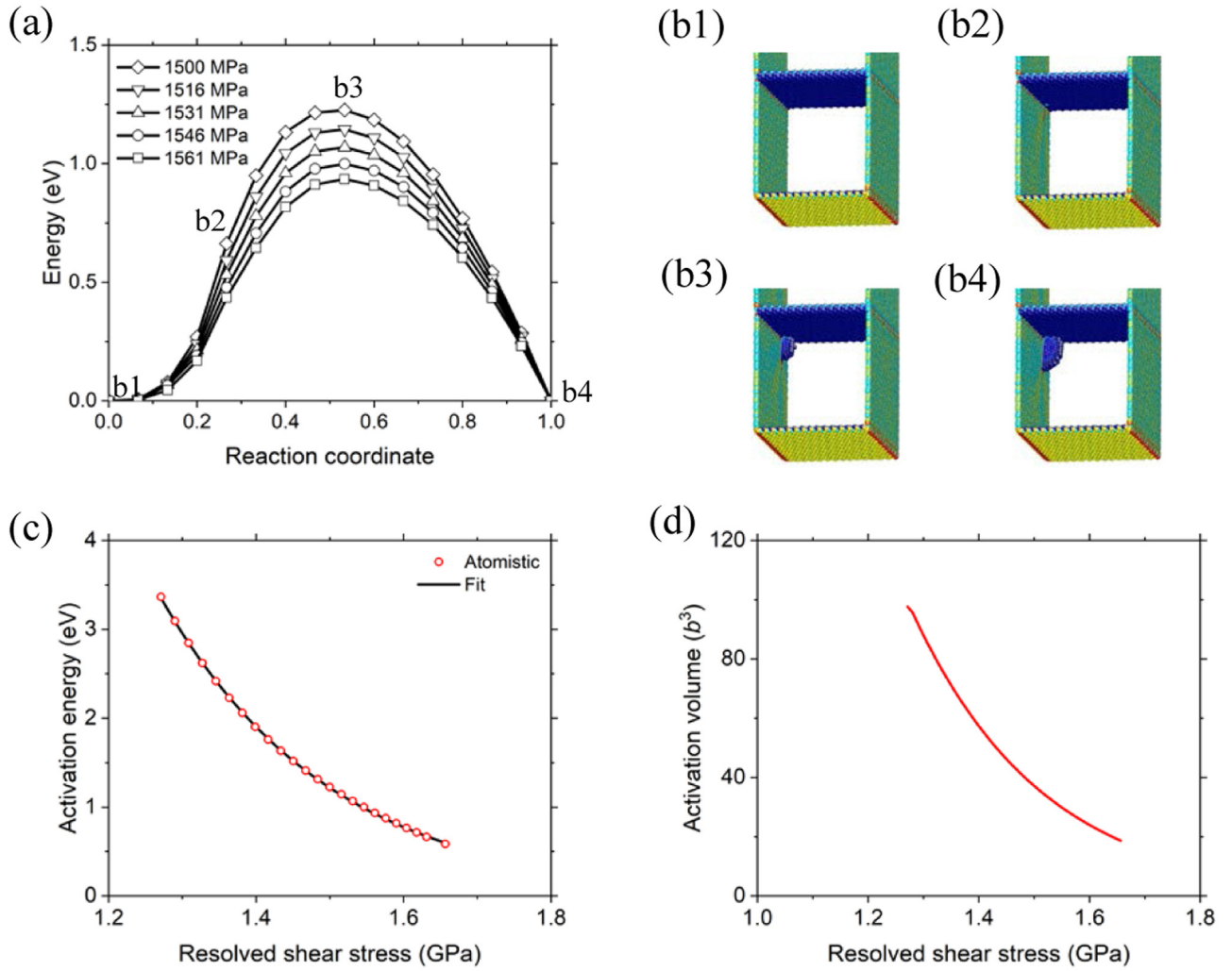


Fig. 7. FENE results of GB dislocation nucleation in an Al bi-crystal. (a) MEPs at different applied resolved shear stresses. (b1-b4) Atomic configurations along the MEP, marked in (a), at an applied resolved shear stress of 1500 MPa. (c) Activation energy as a function of resolved shear stress. Circles show the FENE results and the solid line is the fitting curve. (d) Activation volume as a function of resolved shear stress.

Overall, a key finding from these FENE results is that both surface and GB dislocation nucleation are associated with activation volumes larger than $10b^3$ at $E_{\text{act}} = 0.7$ eV. Implications of these results will be discussed below.

4. Discussion

Theoretical analysis of activation volume. Compared to atomistic FENE calculations, the theoretical modeling of activation energy and activation volume for dislocation nucleation [21,22,24] can provide additional insight into physical factors governing the surface and GB nucleation processes. Here we adapt a theoretical model of dislocation nucleation [21] to analyze the effect of material properties on the activation volume of dislocation nucleation. Focusing on the same surface nucleation mode in atomistic modeling, we consider a quarter of a circular partial dislocation loop emanating from the nanowire corner under an applied shear stress τ . The loop has radius r and core width δ . To a first approximation, we use the isotropic elastic constant of shear modulus μ and neglect the difference between the full and partial Burgers vector lengths. The increase of the system energy associated with loop

nucleation is given by [21]

$$E(r, \tau) = A\mu b^2 r \ln \frac{r}{\delta} - \frac{\pi r^2}{4} \tau b + \frac{\pi r^2}{4} \gamma_{\text{SF}} \quad (4)$$

In Eq. (4), the first term represents the self-energy of the loop, the second term is the work done by τ over the area swept by the loop, and the third term is the energy of the stacking fault enclosed by the loop. The self-energy term involves a dimensionless parameter A , and b is the Burgers vector length. The surface step formation energy is relatively small and thus ignored in this model. The maximum of $E(r, \tau)$ is the activation energy of dislocation loop nucleation. It can be determined by $\partial E / \partial r|_{r=r_c} = 0$, where r_c denotes the critical radius of the loop at the saddle-point state. Such activation energy can be expressed in terms of r_c as

$$E_{\text{act}} = \frac{1}{2} \alpha \mu b^3 \frac{r_c}{b} \left(\ln \frac{r_c}{\delta} - 1 \right) \quad (5)$$

and the corresponding activation volume is

$$\frac{V_{\text{mod}}}{b^3} = \frac{\pi}{4} \left(\frac{r_c}{b} \right)^2 \quad (6)$$

Note that E_{act} in Eq. (5) is an implicit function of τ , because r_c depends on τ . Since the $\ln(r_c/\delta)$ term in Eq. (5) varies slowly with

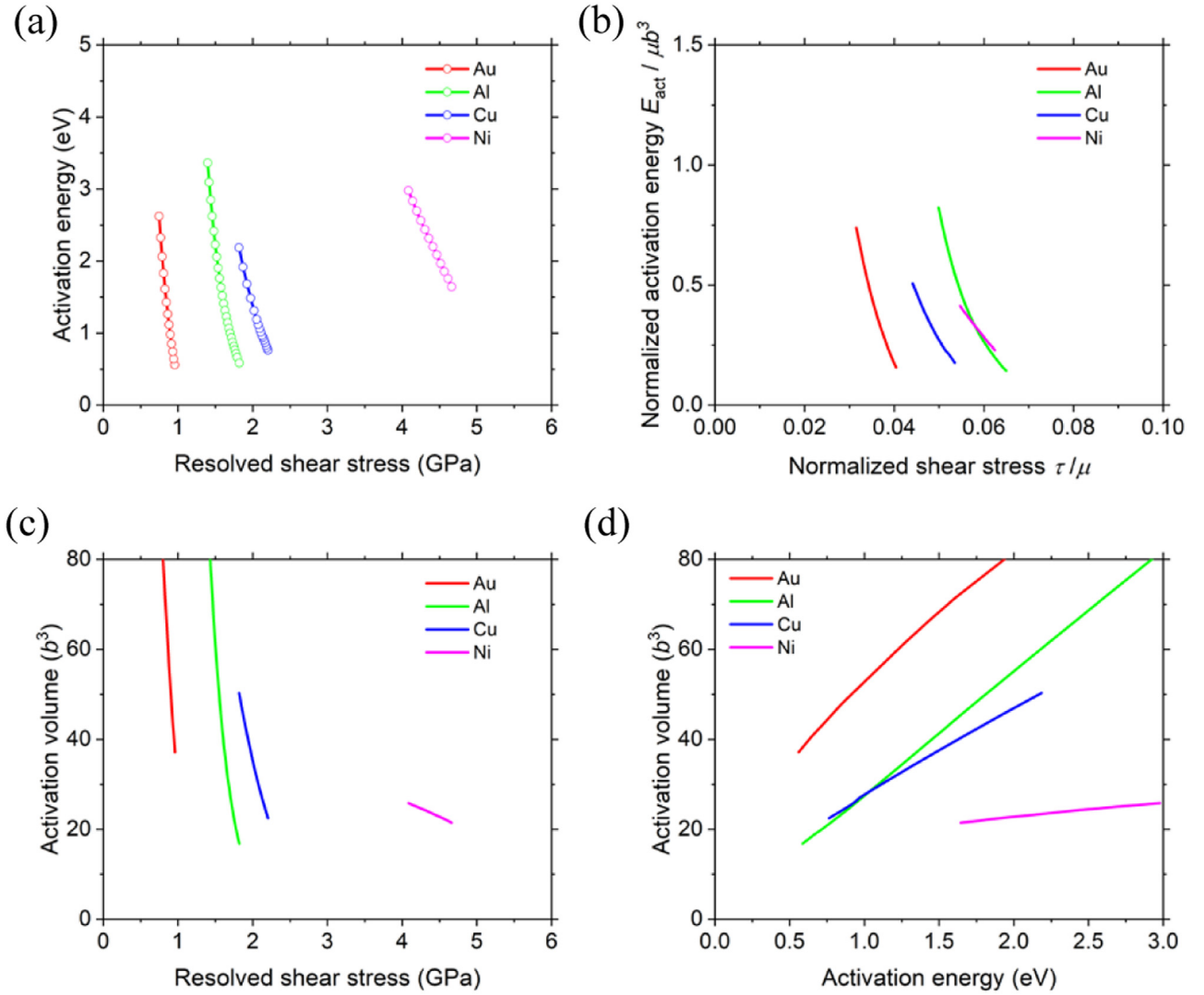


Fig. 8. Comparison of FENE results for GB dislocation nucleation in Al, Au, Cu, and Ni. (a) Activation energy E_{act} vs. resolved shear stress τ . Circles represent the FENE results and solid lines are the fitting curves. (b) Normalized activation energy $E_{act}/\mu b^3$ vs. normalized shear stress τ/μ . (c) Activation volume V_{mod}/b^3 vs. resolved shear stress τ . (d) Activation volume V_{mod}/b^3 vs. activation energy E_{act} .

r_c , it can be treated approximately as a constant. Hence, Eq. (5) indicates that to reach a specific E_{act} value (e.g., 0.7 eV), the material with a lower μb^3 requires a larger critical loop size r_c , thus giving a larger activation volume V_{mod} according to Eq. (6). On this basis, we can use the material properties of the four metals in Table 1 to rationalize the trend of atomistically-determined activation volumes for surface and GB dislocation nucleation. Namely, to reach a specific E_{act} , the decreasing μb^3 from Ni, Cu, Al to Au gives increasing r_c and thus increasing V_{mod} . This theoretical prediction agrees with the trend of the atomistically-determined V_{mod} vs. E_{act} curves of surface dislocation nucleation in Fig. 5(d). The above analysis can be applied approximately to GB dislocation nucleation and also captures the trend of the atomistically-determined V_{mod} vs. E_{act} curves in Fig. 8(d). Note that the variation of μ is much larger than b among the typical FCC metals studied (Table 1). Hence, the shear modulus has a predominant influence on activation volume. As discussed earlier, Al can deviate from these trends to some degree, due to its unusually strong directional bonding and resultant abnormal shear stress-strain behavior [36] compared to the other three FCC metals.

Effect of grain size on activation volume. Experimentally measured activation volumes of polycrystalline materials com-

monly exhibit grain size dependence [12]. It is challenging to use atomistic NEB simulations for exploring the grain size effect on activation volume because realistic polycrystal models spanning a large range of grain sizes would require unaffordable computational resources. To address this challenge, theoretical models have been developed to illuminate the grain size dependence of activation volume [15,37]. The key to these models is to connect an applied far-field stress to an amplified local stress at the GB where the rate-controlling dislocation process is activated. This connection is essential for linking the experimentally measured activation volumes from large polycrystals to the NEB-calculated activation volumes from small atomic systems.

To account for the grain size dependence of activation volume, we use the Conrad model [15,37] that evaluates the amplified local stress at the GB by considering the pileup of a dislocation array against this GB. Since the number of dislocations in the pileup is proportional to grain size d , Conrad showed that the activation volume V for a polycrystal exhibits a Hall-Petch like relation,

$$\frac{1}{V} = \frac{1}{V_i} + \frac{M^2 \mu b}{2\pi \alpha K_{HP} \sqrt{d}} \frac{1}{V_c} \quad (7)$$

where V_i is the activation volume of a rate-controlling process inside grains such as cutting of forest dislocations by glide dislocations, V_c is the activation volume of a rate-controlling process at GBs, K_{H-P} is the Hall-Petch coefficient for characterizing the grain size dependence of yield stress, M is the Taylor factor, and α is the dimensionless parameter in the dislocation pileup model. Inside grains, V_i usually scales with lb^2 , where l is the average spacing between forest junctions obstructing glide dislocations [38,39]. For a typical dislocation density of 10^{14} m^{-2} , $V_i \approx 500b^3$. If GB dislocation nucleation is a rate-controlling process, V_c can be taken as V_{mod} from the NEB results of GB dislocation nucleation. Since V_c is much smaller than V_i , Eq. (7) indicates that decreasing d reduces V , which is consistent with experimental results [15,37]. The lower bound of V corresponds to the case of d approaching its lower limit of ~ 10 nm. To understand this lower bound, we note that as d approaches 10 nm, the applied stress acts directly on GBs as in our FENEb simulations, such that $V \approx V_c \approx V_{\text{mod}}$. Hence, for ultrafine-grained and nanocrystalline FCC metals with decreasing grain sizes toward 10 nm, their activation volumes should be increasingly dominated by GB dislocation nucleation and thus approach $V_c \approx V_{\text{mod}}$, which is no less than $10b^3$ (the lowest value corresponding to $E_{\text{act}} = 0.7$ eV among the four metals from our FENEb results).

By experimental measurements at room temperature, Stangebye et al. [20] reported activation volumes of $\sim 10b^3$ for ultrafine-grained Au thin films with an average grain size of ~ 150 nm; Karanjanagar et al. [17] reported activation volumes of $6.4b^3$ for nanocrystalline Au thin films with the average grain size of 64 nm under low strain rates. These results imply that the activation volumes for nanocrystalline Au with decreasing grain sizes toward 10 nm would be even smaller than $10b^3$, which contradict the above lower bound of $50b^3$ for Au assuming the rate-controlling GB process is GB dislocation nucleation. Hence, the operation of other rate-controlling mechanisms with small activation volumes less than $10b^3$ would be necessary in ultrafine-grained and nanocrystalline FCC metals, particularly for grain sizes less than 100 nm.

Other potential rate-controlling mechanisms. To identify the rate-controlling mechanisms giving small activation volumes less than $10b^3$, we consider various possible processes of GB disconnections leading to GB sliding and/or migration [40]. In general, a GB disconnection is characterized by a non-zero GB step height and GB Burgers vector; if the step height is zero, a disconnection is a pure GB dislocation. Atomistic modeling indicates that the glide of a GB disconnection with zero Burgers vector component perpendicular to the GB experiences little resistance to its motion [41] and thus is unlikely to serve as the rate-limiting process. However, if a GB disconnection has non-zero Burgers vector component perpendicular to the GB, the movement of this disconnection must involve climb motion at the GB. Climb of a GB disconnection requires atomic diffusive processes at its core through migration of point defects toward/away from the GB [40]. Diffusive MD simulations indicate disconnection climb on GBs with the aid of point defects could give small activation volumes of $\sim 1b^3$ [42], which contrast with the even smaller activation volumes of $\sim 0.1b^3$ associated with migration of point defects, e.g., vacancies, in crystal lattices [3]. In other words, while the displacive processes of GB dislocations/disconnections give relatively large activation volumes no less than $10b^3$, the diffusive processes facilitating GB disconnection climb and/or other similar processes of diffusion-mediated dislocation nucleation could give small activation volumes around $1b^3$. Hence, Eq. (7) needs to be modified to take into account the contribution from some rate-controlling diffusive GB processes, so that the effective activation volume V can attain values less than $10b^3$ for ultrafine-grained and nanocrystalline FCC metals. The detailed form of modified Eq. (7) needs further study through

a combination of experimental and modeling efforts in the future.

5. Concluding remarks

We have performed atomistic FENEb calculations to determine the activation energies and activation volumes for surface and GB dislocation nucleation in four typical FCC metals of Al, Ni, Cu and Au. A key finding is that the activation volumes for displacive dislocation nucleation at the surface and GB are larger than $10b^3$ under typical experimental loading conditions. Comparison of the four FCC metals indicates that the shear modulus strongly influences the activation volume values and a metal with higher shear modulus μ gives lower activation volume. This trend is further rationalized by a theoretical model which attributes μb^3 as the main factor governing the activation volumes associated with surface and GB dislocation nucleation. Considering the variation of μ is much larger than b among the typical FCC metals studied, the shear modulus has a predominant influence on the activation volume. Since the theoretical model involves parameters such as dislocation core width that are difficult to evaluate accurately, the quantification of activation volumes requires high-fidelity atomistic calculations, as enabled by the FENEb method in this work.

To compare the atomistically determined activation volumes with the experimentally measured values from polycrystalline materials, it is necessary to account for the amplification of local stress at a GB relative to the applied stress on a polycrystal. To this end, we invoke the Conrad model [15,37] giving a Hall-Petch-like relation of grain size dependent activation volumes. A combination of atomistically determined activation volumes and the Hall-Petch-like relation indicates that for ultrafine-grained and nanocrystalline FCC metals with decreasing grain sizes toward 10 nm, their activation volumes should approach the lower limit of $10b^3$ if the dominant rate-controlling mechanism is GB dislocation nucleation. Such a lower bound is larger than recent experimental results from ultrafine-grained and nanocrystalline FCC metals with decreasing grain sizes less than 100 nm. This discrepancy implies the operation of rate-controlling diffusive processes associated with GB disconnections that likely give small activation volumes less than $10b^3$. These diffusive processes associated with GB disconnections could be greatly enhanced even at room temperature due to the prevailing high stresses in nanograined FCC metals. Further studies are required to resolve this discrepancy.

Broadly speaking, our work demonstrates the advantage of FENEb calculations for studying the stress-driven, thermally-activated dislocation processes relevant to typical experimental loading conditions. Quantitative comparison between the experimental and modeling results of activation volumes shows great promises to determine the rate-controlling deformation mechanisms that would be difficult to clarify by other approaches. Recent implementation of the FENEb method in LAMMPS [30], in conjunction with the comprehensive case studies provided in this work, can facilitate the wide adoption of this combined experimental and modeling approach in future studies. In the same vein, similar displacive dislocation processes as well as other diffusive dislocation processes in metals and alloys with different crystal structures can be investigated. In this work, we focus on the dislocation nucleation processes from atomically sharp GBs. This type of sharp GBs is often observed in ultrafine-grained and nanocrystalline metals. GBs in real polycrystals often have more complex structures with preexisting defects such as GB dislocations and disconnections [43] and may be locally disordered [44]. The activation energies and activation volumes associated with these complex GBs warrant further studies by the NEB method and other advanced modeling approaches for atomic-scale rare events [45–48] in the future. Such comprehensive studies will deepen our understand-

ing of atomistically-governed plastic deformation kinetics in metals and alloys, which is essential to the control of time-dependent mechanical behavior of advanced materials.

Declaration of Competing Interest

The authors declare that they have no known competing financial interests or personal relationships that could have appeared to influence the work reported in this paper.

Acknowledgments

This work is supported by the [U.S. Department of Energy \(DOE\)](#), Office of Science, Basic Energy Sciences (BES) Materials Science and Engineering (MSE) Division under Award #DE-SC0018960.

References

- [1] A.S. Argon, *Strengthening Mechanisms in Crystal Plasticity*, Oxford University Press Inc., New York, 2008.
- [2] G. Caillard, J.L. Martin, *Thermally Activated Mechanisms in Crystal Plasticity*, Pergamon, 2003.
- [3] T. Zhu, J. Li, Ultra-strength materials, *Prog. Mater. Sci.* 55 (2010) 710–757.
- [4] J.R. Greer, J.T.M. De Hosson, Plasticity in small-sized metallic systems: intrinsic versus extrinsic size effect, *Prog. Mater. Sci.* 56 (6) (2011) 654–724.
- [5] A.H. Cottrell, The Nabarro equation for thermally activated plastic glide, *Philos. Mag.* 86 (25–26) (2006) 3811–3817.
- [6] T. Zhu, J. Li, S. Yip, Atomistic reaction pathway sampling: the nudged elastic band method and nanomechanics applications, in: H.D. Espinosa, G. Bao (Eds.), *Nano and Cell Mechanics*, John Wiley & Sons 2013, pp. 313–338.
- [7] G.H. Vineyard, Frequency factors and isotope effects in solid state rate processes, *J. Phys. Chem. Solids* 3 (1–2) (1957) 121–127.
- [8] H. Jonsson, G. Mills, K.W. Jacobsen, Nudged elastic band method for finding minimum energy paths of transitions In B. J. Berne, G. Ciccotti, and D. F. Coker, editors, *Classical and Quantum Dynamics in Condensed Phase Simulations* (1998) 385–404.
- [9] T. Zhu, J. Li, S. Yip, Atomistic study of dislocation loop emission from a crack tip, *Phys. Rev. Lett.* 93 (2004) 025503.
- [10] T. Zhu, J. Li, A. Samanta, H.G. Kim, S. Suresh, Interfacial plasticity governs strain rate sensitivity and ductility in nanostructured metals, *Proc. Natl Acad. Sci. USA* 104 (9) (2007) 3031.
- [11] T. Zhu, J. Li, A. Samanta, A. Leach, K. Gall, Temperature and strain-rate dependence of surface dislocation nucleation, *Phys. Rev. Lett.* 100 (2) (2008) 025502.
- [12] L. Lu, R. Schwaiger, Z.W. Shan, M. Dao, K. Lu, S. Suresh, Nano-sized twins induce high rate sensitivity of flow stress in pure copper, *Acta Mater.* 53 (7) (2005) 2169–2179.
- [13] Y.M. Wang, A.V. Hamza, E. Ma, Temperature-dependent strain rate sensitivity and activation volume of nanocrystalline Ni, *Acta Mater.* 54 (10) (2006) 2715–2726.
- [14] J.K. Mason, A.C. Lund, C.A. Schuh, Determining the activation energy and volume for the onset of plasticity during nanoindentation, *Phys. Rev. B* 73 (5) (2006) 054102.
- [15] H. Conrad, Plastic deformation kinetics in nanocrystalline FCC metals based on the pile-up of dislocations, *Nanotechnology* 18 (32) (2007) 325701.
- [16] K. Jonnalagadda, N. Karanjgaokar, I. Chasiotis, J. Chee, D. Peroulis, Strain rate sensitivity of nanocrystalline Au films at room temperature, *Acta Mater.* 58 (14) (2010) 4674–4684.
- [17] N.J. Karanjgaokar, C.S. Oh, J. Lambros, I. Chasiotis, Inelastic deformation of nanocrystalline Au thin films as a function of temperature and strain rate, *Acta Mater.* 60 (13) (2012) 5352–5361.
- [18] S. Gupta, S. Stangebye, K. Jungjohann, B. Boyce, T. Zhu, J. Kacher, O.N. Pierron, In situ TEM measurement of activation volume in ultrafine grained gold, *Nanoscale* 12 (13) (2020) 7146–7158.
- [19] S. Gupta, S. Stangebye, K. Jungjohann, B. Boyce, T. Zhu, J. Kacher, O.N. Pierron, Correction: in situ TEM measurement of activation volume in ultrafine grained gold, *Nanoscale* 13 (19) (2021) 9040–9040.
- [20] S. Stangebye, Y. Zhang, S. Gupta, T. Zhu, O. Pierron, J. Kacher, Understanding and quantifying electron beam effects during in situ TEM nanomechanical tensile testing on metal thin films, *Acta Mater.* 222 (2022) 117441.
- [21] A.H. Cottrell, *Dislocations and Plastic Flow in Crystals*, Oxford University Press, London, 1953.
- [22] G. Xu, A.S. Argon, Homogeneous nucleation of dislocation loops under stress in perfect crystals, *Philos. Mag. Lett.* 80 (9) (2000) 605–611.
- [23] D.H. Warner, W.A. Curtin, S. Qu, Rate dependence of crack-tip processes predicts twinning trends in f.c.c. metals, *Nat. Mater.* 6 (2007) 876–881.
- [24] S. Aubry, K. Kang, S. Ryu, W. Cai, Energy barrier for homogeneous dislocation nucleation: comparing atomistic and continuum models, *Scr. Mater.* 64 (11) (2011) 1043–1046.
- [25] L. Proville, D. Rodney, M.-C. Marinica, Quantum effect on thermally activated glide of dislocations, *Nat. Mater.* 11 (2012) 845–849.
- [26] C.R. Weinberger, A.T. Jennings, K. Kang, J.R. Greer, Atomistic simulations and continuum modeling of dislocation nucleation and strength in gold nanowires, *J. Mech. Phys. Solid.* 60 (1) (2012) 84–103.
- [27] A.T. Jennings, C.R. Weinberger, S.-W. Lee, Z.H. Aitken, L. Meza, J.R. Greer, Modeling dislocation nucleation strengths in pristine metallic nanowires under experimental conditions, *Acta Mater.* 61 (6) (2013) 2244–2259.
- [28] Z. Wu, W.A. Curtin, The origins of high hardening and low ductility in magnesium, *Nature* 526 (7571) (2015) 62–67.
- [29] Q.-J. Li, B. Xu, S. Hara, J. Li, E. Ma, Sample-size-dependent surface dislocation nucleation in nanoscale crystals, *Acta Mater.* 145 (2018) 19–29.
- [30] S. Plimpton, Fast parallel algorithms for short-range molecular-dynamics, *J. Comput. Phys.* 117 (1) (1995) 1–19.
- [31] X.W. Zhou, R.A. Johnson, H.N.G. Wadley, Misfit-energy-increasing dislocations in vapor-deposited CoFe/NiFe multilayers, *Phys. Rev. B* 69 (14) (2004) 144113.
- [32] S.M. Foiles, M.I. Baskes, M.S. Daw, Embedded-atom-method functions for the fcc metals Cu, Ag, Au, Ni, Pd, Pt, and their alloys, *Phys. Rev. B* 33 (12) (1986) 7983–7991.
- [33] Y. Mishin, D. Farkas, M.J. Mehl, D.A. Papaconstantopoulos, Interatomic potentials for monoatomic metals from experimental data and ab initio calculations, *Phys. Rev. B* 59 (5) (1999) 3393–3407.
- [34] Y. Mishin, M.J. Mehl, D.A. Papaconstantopoulos, A.F. Voter, J.D. Kress, Structural stability and lattice defects in copper: Ab initio, tight-binding, and embedded-atom calculations, *Phys. Rev. B* 63 (22) (2001) 224106.
- [35] J. Li, AtomEye: an efficient atomistic configuration viewer, *Model. Simul. Mater. Sci. Eng.* 11 (2) (2003) 173–177.
- [36] S. Ogata, J. Li, S. Yip, Ideal pure shear strength of aluminum and copper, *Science* 298 (5594) (2002) 807–811.
- [37] H. Conrad, Grain size dependence of the plastic deformation kinetics in Cu, *Mater. Sci. Eng.* 341 (1) (2003) 216–228.
- [38] F.R.N. Nabarro, Cottrell-stokes law and activation theory, *Acta Metall. Mater.* 38 (2) (1990) 161–164.
- [39] D. Chen, L.L. Costello, C.B. Geller, T. Zhu, D.L. McDowell, Atomistic modeling of dislocation cross-slip in nickel using free-end nudged elastic band method, *Acta Mater.* 168 (2019) 436–447.
- [40] D. Hull, D.J. Bacon, *Introduction to Dislocations*, Butterworth-Heinemann, 2001.
- [41] D. Chen, S. Xu, Y. Kulkarni, Atomistic mechanism for vacancy-enhanced grain boundary migration, *Phys. Rev. Mater.* 4 (3) (2020) 033602.
- [42] S. Sarkar, J. Li, W.T. Cox, E. Bitzek, T.J. Lenosky, Y. Wang, Finding activation pathway of coupled dislocation-diffusion defect processes in atomistics: dislocation climb in fcc copper, *Phys. Rev. B* 86 (1) (2012) 014115.
- [43] L. Wang, Y. Zhang, Z. Zeng, H. Zhou, J. He, P. Liu, M. Chen, J. Han, D.J. Srolovitz, J. Teng, Y. Guo, G. Yang, D. Kong, E. Ma, Y. Hu, B. Yin, X. Huang, Z. Zhang, T. Zhu, X. Han, Tracking the sliding of grain boundaries at the atomic scale, *Science* 375 (6586) (2022) 1261–1265.
- [44] Z. Bai, G.H. Balbus, D.S. Gianola, Y. Fan, Mapping the kinetic evolution of metastable grain boundaries under non-equilibrium processing, *Acta Mater.* 200 (2020) 328–337.
- [45] G. Henkelman, H. Jónsson, Long time scale kinetic Monte Carlo simulations without lattice approximation and predefined event table, *J. Chem. Phys.* 115 (21) (2001) 9657–9666.
- [46] Y. Fan, T. Iwashita, T. Egami, Energy landscape-driven non-equilibrium evolution of inherent structure in disordered material, *Nat. Commun.* 8 (1) (2017) 15417.
- [47] C. Liu, X. Yan, P. Sharma, Y. Fan, Unraveling the non-monotonic ageing of metallic glasses in the metastability-temperature space, *Comput. Mater. Sci.* 172 (2020) 109347.
- [48] Y. Feng, J. Fan, E.B. Tadmor, A rigorous universal model for the dynamic strength of materials across loading rates, *J. Mech. Phys. Solids* 159 (2022) 104715.